Re-entrant spin reorientation transition and Griffiths-like phase in antiferromagnetic $TbFe_{0.5}Cr_{0.5}O_3$

Bhawana Mali,[1,*] Harikrishnan S. Nair,[2] T. W. Heitmann,[3] Hariharan Nhalil,[1,†] Daniel Antonio,[4] Krzysztof Gofryk,[4] Shalika Ram Bhandari,[5,6] Madhav Prasad Ghimire,[5,6] and Suja Elizabeth[1]

[1]*Department of Physics, Indian Institute of Science, Bangalore 560012, India*
[2]*Department of Physics, 500 W. University Ave., The University of Texas at El Paso, Texas 79968, USA*
[3]*The Missouri Research Reactor, University of Missouri, Columbia, Missouri 65211, USA*
[4]*Idaho National Laboratory, Idaho Falls, Idaho 83415, USA*
[5]*Central Department of Physics, Tribhuvan University, Kirtipur, 44613 Kathmandu, Nepal*
[6]*IFW Dresden, Helmholtzstr. 20, D-01069 Dresden, Germany*

(Received 14 January 2020; revised 17 June 2020; accepted 24 June 2020; published 13 July 2020)

The perovskite $TbFe_{0.5}Cr_{0.5}O_3$ shows two anomalies in its magnetic susceptibility at $T_N = 257$ K and $T_{SR} = 190$ K which are, respectively, the antiferromagnetic and spin-reorientation transition that occur in the Fe/Cr sublattice. Magnetic susceptibility of this compound reveals canonical signatures of a Griffiths-like phase: a negative deviation from the ideal Curie-Weiss law and in less-than-unity power-law susceptibility exponents. Neutron-diffraction data analysis confirms two spin-reorientation transitions in this compound. The first one from Γ_2 (C_x, G_y, F_z) to Γ_4 (A_x, F_y, G_z) occurs at $T_N = 257$ K and a second one from Γ_4 (A_x, F_y, G_z) to Γ_2 (C_x, G_y, F_z) at $T_{SR} = 190$ K in the *Pnma* space-group setting. The Γ_2 (C_x, G_y, F_z) structure is stable down to 7.7 K, leading to an ordered moment of 3.34(1) $\mu_B/Fe^{3+}(Cr^{3+})$. In addition to the long-range magnetic order, experimental indication of diffuse magnetism is observed in neutron-diffraction data at 7.7 K. Tb develops a ferromagnetic component along the z axis at 20 K. Thermal conductivity and spin-phonon coupling of $TbFe_{0.5}Cr_{0.5}O_3$ studied through Raman spectroscopy are also presented in the paper. The magnetic anomalies at T_N and T_{SR} do not appear in the thermal conductivity of $TbFe_{0.5}Cr_{0.5}O_3$, which appears to be robust up to 9 T. On the other hand, they are revealed in the temperature dependence of full-width-at-half-maximum curves derived from Raman intensities. An antiferromagnetic structure with ↑↓↑↓ arrangement of Fe/Cr spins is found as the ground state through first-principles energy calculations, supporting the experimentally determined magnetic structure at 7.7 K. The spin-resolved total and partial density of states show that $TbFe_{0.5}Cr_{0.5}O_3$ is insulating with a band gap of ∼0.12 (2.4) eV within GGA (GGA+U) functionals.

DOI: 10.1103/PhysRevB.102.014418

I. INTRODUCTION

Rare-earth orthoferrites and orthochromites with the general formula RMO_3, where R = rare earth or yttrium and M = Fe or Cr, crystallize in the perovskite structure (usually *Pnma* space group) with orthorhombic distortion and an antiferromagnetic ground state [1]. Rare-earth orthoferrites possess a complex spin structure and have drawn considerable attention due to their unique physical properties [1] and potential applications such as ultrafast magneto-optical recording [2], laser-induced thermal spin reorientation (SR) [3], precision excitation induced by terahertz pulses [4], inertia-driven spin switching [5], and magnetism-induced multiferroicity [6]. Most orthoferrites are G–type canted antiferromagnets with a weak ferromagnetic (FM) component due to Dzyaloshinskii-Moriya interaction and show temperature-induced SR from one magnetic symmetry to another. In $RFeO_3$, exchange interactions between Fe^{3+}– Fe^{3+}, R^{3+}–Fe^{3+}, and R^{3+}–R^{3+} play an important role in determining complex magnetic structures. Isotropic Fe^{3+}–Fe^{3+} exchange interaction determines the magnetic structure of Fe^{3+} spins below the antiferromagnetic ordering temperature. An exchange field due to the Fe^{3+} moment polarizes the R^{3+} spins of the R sublattice and the Fe^{3+}–R^{3+} interaction, in turn, generating effective fields on Fe^{3+} spins which undergo SR transition and align perpendicular to the R^{3+} spins. The SR transition might be continuous or abrupt depending on the R element [7].

In $TbFeO_3$, an unusual incommensurate magnetic phase was discovered [8] and it was shown that the exchange of spin waves between extended topological defects could result in novel magnetic phases which draws parallels with the Yukawa forces that mediate between protons and neutrons in a nucleus. The Fe^{3+} moments in $TbFeO_3$ exhibit $A_xF_yG_z$ ($Pn'ma'$) spin configuration at room temperature [9–11] which is accompanied by a SR to $C_xG_yF_z$ ($Pn'm'a$). At 3 K, another SR occurs to revert to the $A_xF_yG_z$ ($Pn'ma'$) structure. In recent years, a variety of interesting properties were achieved by substituting an Fe ion by different transition metal ions [12,13]. According to Goodenough-Kanamori rules [14], Cr^{3+} is a good choice to pair with Fe^{3+} to tune superior magnetic properties due to

*Corresponding author: bhawana@iisc.ac.in
†Present address: Department of Physics, Bar-Ilan University, Ramat-Gan 5290002, Israel.

superexchange interaction between empty e_g orbitals of Cr^{3+} and half-filled e_g orbitals of Fe^{3+} ions.

In $TbCrO_3$, the exchange coupling between the nearest-neighbor Cr^{3+} is predominantly antiferromagnetic and the Cr^{3+} spins order spontaneously at $T_N = 167$ K [15]. Below this temperature, it exhibits weak ferromagnetism resulting from the canting of Cr^{3+} magnetic moments. In $TbCrO_3$, the Cr^{3+} spin structure is G_yF_z below T_N and belongs to the Γ_2 configuration, which implies that a weak FM component of the Cr^{3+} moments orient along the z axis [16,17]. Tb^{3+} spins order antiferromagnetically at 3.05 K into a G_xA_z structure [16]. The Tb^{3+} spin system adopts a C_xF_z structure, which belongs to Γ_4 representation, in the temperature range 3.05 K $< T < T_N$ and is coupled to the ordered Cr^{3+} spins [16]. Spin reorientation, magnetization reversal, and weak ferromagnetism are often seen in similar compounds, for example, $TbFe_{0.5}Mn_{0.5}O_3$ [18], while a reentrant SR transition is reported in $TbFe_{0.75}Mn_{0.25}O_3$ [19] which transforms from Γ_4 to Γ_1 and subsequently to Γ_4. The magnetic structures and SR transitions of the mixed orthochromite–orthoferrite perovskites $RFe_{0.5}Cr_{0.5}O_3$, where R = Tb, Dy, Ho, Er have recently been reported [20].

In this paper, we present a comprehensive understanding of the magnetism of $TbFe_{0.5}Cr_{0.5}O_3$ through magnetic susceptibility, neutron powder diffraction, Raman scattering, and thermal conductivity experiments in conjunction with density-functional-theory calculations. Our results support a reentrant SR transition, Griffiths-like phase features, and a coexisting diffuse magnetic component below the T_N.

II. METHODS

A. Experimental

Polycrystalline $TbFe_{0.5}Cr_{0.5}O_3$ was prepared by a standard solid-state reaction using high purity ($\geqslant 3N$) Tb_4O_7, Fe_2O_3, and Cr_2O_3 in stoichiometric amounts. The starting materials were thoroughly mixed and sintered at 1200 °C for 48 h with two stages of intermediate grinding. Phase purity of the sintered sample was verified by taking powder x-ray diffractograms using a Rigaku Smartlab x-ray diffractometer with Cu K_α radiation ($\lambda = 1.548$ Å). Oxidation states of Fe and Cr ions were determined using x-ray photoelectron spectroscopy (XPS) in an AXIS Ultra spectrometer, and the data were analyzed using CASA XPS spectroscopy software [21]. Chemical composition analysis of the samples were performed using a JEOL–JXA–8530F electron probe micro analyzer, which yielded the Fe:Cr atomic ratio as 0.48:0.50 (Fe/Cr = 0.96). Temperature-dependent DC magnetization measurements were performed on sintered pellets using a commercial magnetic property measurement system (Quantum Design) in the temperature range of 5 K $\leqslant T \leqslant$ 400 K at 100 Oe and 500 Oe in both zero-field-cooled (ZFC) and field-cooled (FC) protocols. Additionally, high-temperature magnetic susceptibility was recorded up to 800 K in the high-temperature vibrating sample magnetometer (VSM) oven option of a physical property measurement system (PPMS). The thermal conductivity of a parallelopiped sample of $TbFe_{0.5}Cr_{0.5}O_3$ was measured in the temperature range 2 K–300 K in 0 T and 9 T magnetic field using a commercial PPMS.

To investigate the nuclear and magnetic structure of $TbFe_{0.5}Cr_{0.5}O_3$, neutron powder diffraction experiments were performed at University of Missouri Research Reactor using the diffractometer, PSD. Patterns were collected at 350 K, 300 K, 215 K, 100 K, 20 K and 7.7 K on a 2 g powder sample using neutrons of wavelength 1.485 Å. The neutron-diffraction data were analyzed using the Rietveld method [22] coded in the FullProf suite of programs [23]. Magnetic representations belonging to the *Pnma* symmetry were determined using the software SARA*h* [24] and the corresponding magnetic structure was refined using FullProf. Raman spectra was recorded from 110 K to 300 K temperature range in the backscattering geometry by using a HORIBA JOBIN–YVON spectrometer with a 633-nm laser as an excitation source. Low temperature was maintained by a closed cycle He–cryostat attached to spectrometer.

B. Computational details

The electronic and magnetic structure calculations were performed by means of density-functional-theory (DFT) approach using the full-potential linearized augmented plane wave plus local orbital method as implemented in the WIEN2k code [25]. The nonoverlapping muffin–tin sphere radii (R_{MT}) of 2.35, 2.0, 1.96, and 1.72 Bohr were used for Tb, Fe, Cr, and O, respectively. The linear tetrahedron method with 500 k points was employed for the reciprocal-space integrations in the whole Brillouin zone (BZ) that corresponds to 216 k points within the irreducible BZ. For the calculations, the standard generalized gradient approximation (GGA) in the parametrization of Perdew *et al.* was used [26]. To consider the strong correlation effects, GGA+U functional with double-counting corrections according to Anisimov *et al.* [27] was used. The chosen values of U were 6 eV for Tb–4f, 5 eV for Fe–3d, and 3 eV for Cr–3d states, which are comparable to the values found in literature [28–33]. Calculations were performed using the lattice parameters obtained from neutron-diffraction data at 7.7 K (see Table I). The energy and charge convergence was set to 10^{-6} Ry and 10^{-4} of an electron, respectively, for self–consistent calculations. To obtain the magnetic ground states, we have considered five magnetic configurations by computing their total energies: They are ferromagnetic (FM– ↑↑↑↑), two antiferromagnetic (AFM1– ↑↓↑↓ and AFM2– ↑↓↓↑), and two ferrimagnetic (FIM1– ↑↓↓↓ and FIM2– ↑↑↑↓). Here, the spin arrangements for two inequivalent atoms each of Fe and Cr atoms are arranged as Fe1, Fe2, Cr1, and Cr2, respectively.

III. RESULTS AND DISCUSSION

A. X–ray photoelectron spectroscopy

Core-level XPS measurements at room temperature using an Al K_α x-ray source was performed to determine the valence states of cations in $TbFe_{0.5}Cr_{0.5}O_3$. Since the valence state of elements plays a crucial role in determining the magnetic ground states of a compound, it is important to identify the same. Figure 1 shows the experimental intensities along with the peak fits. The core-level binding energy was calibrated with carbon (B.E = 284.8 eV). The Cr $2p_{3/2}$ peak at 576.5 eV is close to the binding energy of Cr_2O_3 (576 eV)

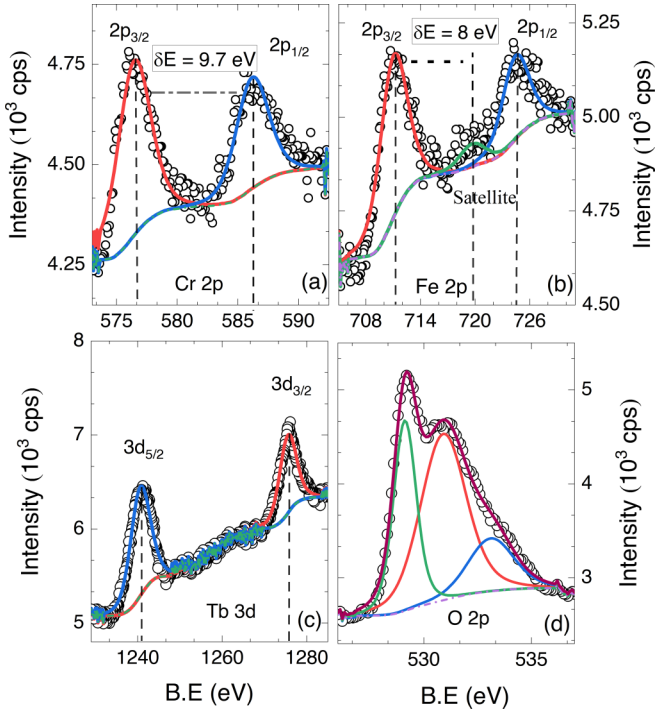

FIG. 1. X–ray photoelectron spectra of (a) Cr $2p$, (b) Fe $2p$, (c) Tb $3d$, and (d) O $2p$ are shown in open circles. Solid lines are fitted peaks, deconvoluted components and background, respectively, in each graph. Oxidation state of 3+ is inferred for Fe, Cr, and Tb from this data.

[34]. However, the $2p_{3/2}$ peaks of Fe^{2+} and Fe^{3+} in oxides appear around 710.3 eV and 711.4 eV, respectively [35]. In $TbFe_{0.5}Cr_{0.5}O_3$, the peak at 711 eV is close to the binding energy value of Fe^{3+}. Additionally, a satellite peak at 8 eV above the Fe $2p_{3/2}$ confirms the Fe^{3+} state (Fe^{2+} gives a satellite peak at 6 eV above the main peak). The XPS spectra of Tb $3d_{5/2}$ yields a peak at 1240.8 eV which is very close to that of Tb_2O_3 (1241.2 eV) [36]. Our XPS results thus indicate 3+ oxidation states in Tb, Fe, and Cr.

B. Magnetic properties: Spin reorientation and Griffiths-like phase

Figure 2(a) shows the temperature-dependent magnetization, $M(T)$, of $TbFe_{0.5}Cr_{0.5}O_3$ under ZFC and FC protocols at 100 Oe and 500 Oe (inset). Two anomalies occur in the $M(T)$ curve at ≈257 K and at 190 K. A bifurcation of the ZFC and FC curves is seen below ≈15 K. With the application of 500 Oe, the bifurcation vanishes [inset of Fig. 2(a)]. The magnetic phase transition temperatures of $TbFe_{0.5}Cr_{0.5}O_3$ are determined as $T_{SR} = 190$ K and $T_N = 257$ K by plotting dM/dT vs T as shown in the top inset of Fig. 2(b). The temperature-dependent inverse magnetic susceptibility, $\chi^{-1}(T)$, of $TbFe_{0.5}Cr_{0.5}O_3$ up to 800 K under 500 Oe is plotted in the main panel of Fig. 2(b) along with a curve fit using the Curie-Weiss (CW) law, shown by a red solid line. The equation $\chi^{-1} = (T–\theta)/C$, where, $C = N_A\mu_{\rm eff}^2/3k_B$ is the Curie constant, N_A is the Avogadro's number, $\mu_{\rm eff}$ is the effective magnetic moment, k_B is the Boltzmann constant, and θ is the CW temperature used for the fit [37]. The CW analysis yields an effective magnetic moment of $\mu_{\rm eff} = 10.3(2)\ \mu_B$ and CW constant, $\theta = -40.4(2)$ K. By taking 3+ oxidation states for Tb, Fe, and Cr determined from the XPS analysis, the theoretical magnetic moment $\mu_{\rm th}$ in the paramagnetic region was calculated using $\mu_{\rm th} = \sqrt{\mu_{\rm Tb}^2 + 0.5\mu_{\rm Cr}^2 + 0.5\mu_{\rm Fe}^2} = 10.9\ \mu_B$ by considering the high-spin state of Tb^{3+} ($\mu_{\rm Tb} = 9.7\ \mu_B$), Fe^{3+} ($\mu_{\rm Fe} = 5.9\ \mu_B$), and Cr^{3+} ($\mu_{\rm Cr} = 3.9\ \mu_B$).

A downward deviation of inverse magnetic susceptibility from the ideal CW law description is a signature of Griffith's phase (GP) [38–40]. The characteristic temperature at which the inverse susceptibility deviates from the CW behavior is

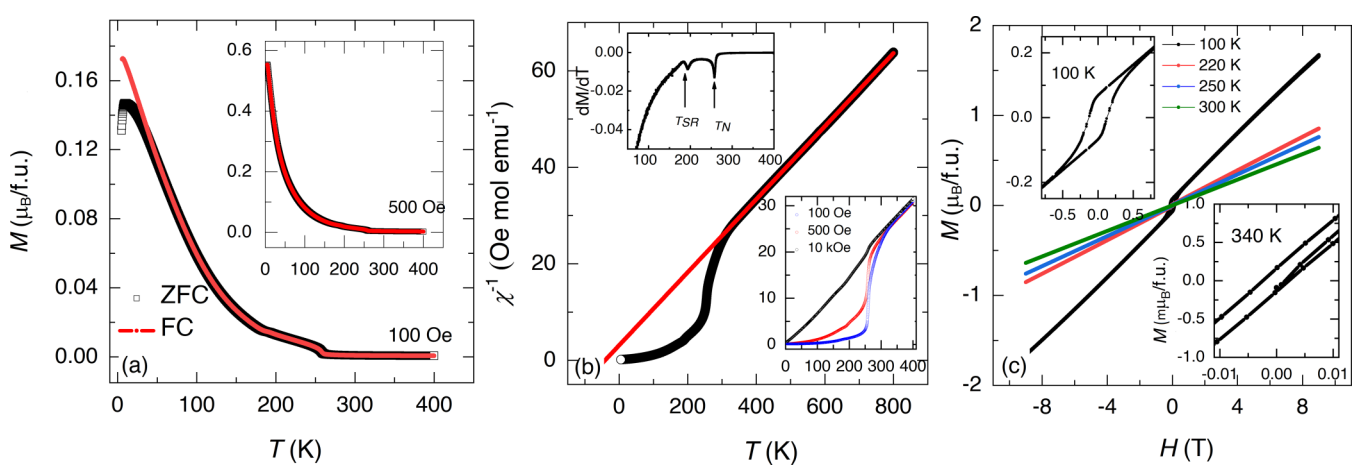

FIG. 2. (a) Magnetization $M(T)$ at 100 Oe shows a bifurcation of ZFC and FC curves and anomalies at $T_N \approx 257$ K and $T_{SR} \approx 190$ K. The inset shows the magnetization at 500 Oe. (b) Inverse susceptibility, $\chi^{-1}(T)$, at 500 Oe along with Curie-Weiss fit (red solid line). The upper inset shows the derivative dM/dT to identify the anomalies at T_N and T_{SR}. The lower inset shows the inverse magnetic susceptibility at 100 Oe, 500 Oe, and 10 kOe, which shows that the negative curvature vanishes at higher fields. (c) The magnetization isotherms, $M(H)$, at 100 K, 220 K, 250 K, and 300 K. A weak hysteresis that develops below the T_{SR} is shown in the upper inset for $T = 100$ K and the lower inset shows a magnified view of an isotherm above the T_N, at $T = 340$ K.

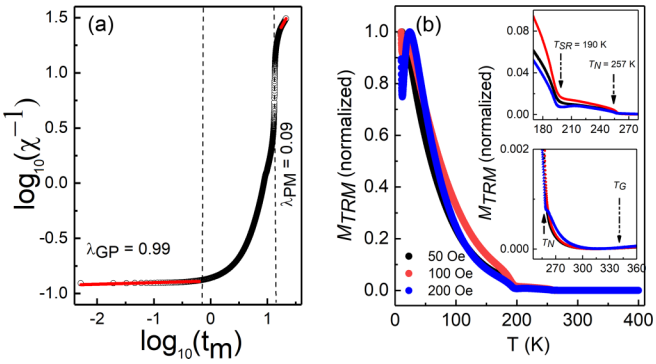

FIG. 3. (a) Power-law fit (red solid lines) to $\chi^{-1}(T)$ at 100 Oe is plotted in a log-log scale. $t_m = (T/T_c^R - 1)$ is the reduced–temperature. (b) Thermoremanant magnetization, M_{TRM}, measured at 50 Oe, 100 Oe, and 200 Oe cooling fields, shows the onset of spin reorientation transition T_{SR} and the antiferromagnetic T_N. The lower and upper insets show magnified regions near the T_N and T_{SR}, respectively.

known as the Griffiths temperature, T_G. Such a deviation of the inverse susceptibility from CW law above T_N at $T_G \approx 340$ K can be seen in Fig. 2(b). The downturn softens with increase in applied magnetic field as can be seen in the lower inset of Fig. 2(b), and supports the presence of Griffiths-like phase.

Figure 2(c) shows the magnetization isotherms of $TbFe_{0.5}Cr_{0.5}O_3$ at 100 K, 220 K, 250 K, 300 K, and 340 K measured up to ±9 T, which do not reveal strong FM features. However, at 100 K, an opening of the magnetic hysteresis loop is observed at low applied field values [upper left inset of Fig. 2(c)]. A magnified view of the isotherm at 340 K ($>T_N$) shown in the lower inset of Fig. 2(c) reveals weak hysteresis that might be suggestive of the presence of short-range magnetism above T_N.

We noted earlier that the softening of the downturn in $\chi^{-1}(T)$ with increasing applied field supported a GP-like scenario [41–43]. At high magnetic fields, the sample gets strongly polarized and hence softens the downturn in $\chi^{-1}(T)$ seen at lower fields. GP consists of finite-size FM clusters in a paramagnetic matrix well above the transition temperature in which the spins are ferromagnetically correlated within those clusters. However, the magnetic system as a whole does not have long-range order in GP, thus, no spontaneous magnetization will appear. In GP, the FM clusters will appear with variable sizes, having local FM ordering due to which magnetization becomes nonanalytic; magnetic susceptibility will follow a power-law behavior in the low-field region [38,41,42] given by $\chi^{-1} \propto (T - T_c^R)^{1-\lambda}$, where T_c^R is the critical temperature of the FM clusters. Here susceptibility tends to deviate from CW law and $\lambda (0 \leqslant \lambda \leqslant 1)$ is the exponent which signifies the deviation from CW behavior due to the formation of magnetic clusters in the paramagnetic (PM) state above the transition temperature. A power-law fit using the above-mentioned equation was administered on the magnetic susceptibility of $TbFe_{0.5}Cr_{0.5}O_3$ plotted as $\log_{10}(\chi^{-1})$ versus $\log_{10}(T/T_c^R - 1)$ in both PM and GP regions as shown in Fig. 3(a). Since the value of λ is highly sensitive to T_c^R, we have proceeded to estimate the value of T_c^R accurately [42,44]. Since the critical temperature of FM clusters, T_c^R, is always greater than the transition temperature, we first estimated the value of T_c^R in the purely PM region. This yields a value of 18 K which was later used in the curve fitting for the GP regime to obtain $\lambda = 0.99(6)$. In the high-temperature region, we obtained λ as 0.09(4) which signifies that the system is in PM phase, following the CW behavior. The values for λ are consistent with the GP model, signifying a Griffiths singularity in $TbFe_{0.5}Cr_{0.5}O_3$.

Since the total magnetic susceptibility in the GP region contains contributions from both PM as well as short-range correlated regions, the downturn observed in the inverse magnetic susceptibility from ideal CW law is not expected to be sharp in the case of antiferromagnetically correlated regions. In $RFeO_3$, five outer shell electrons of Fe^{3+} are in half–filled e_g (σ–bond component) and t_{2g} (π–bond component) orbitals, resulting in superexchange interactions that are antiferromagnetic. In the case of Cr^{3+}, superexchange interactions in the half–filled t^3–O–t^3 induce antiferromagnetism. Since Fe^{3+} and Cr^{3+} are randomly distributed in the lattice of $TbFe_{0.5}Cr_{0.5}O_3$, it results in the stabilization of both FM and antiferromagnetic couplings.

To confirm the GP–like scenario in antiferromagnetic $TbFe_{0.5}Cr_{0.5}O_3$, we employed thermoremanant magnetization, M_{TRM}, protocol to measure magnetization. Such a protocol has been used widely to study spin glass [45]. The protocol involves cooling a sample from well above the magnetic transition temperature in the presence of a magnetic field. The field is then switched off below T_C, and the magnetization measured upon warming in zero-field conditions. The thermoremanent magnetization M_{TRM} will exhibit a sharp upturn at the transition temperature. In the present case of $TbFe_{0.5}Cr_{0.5}O_3$, this protocol was repeated for three different cooling fields, 50 Oe, 100 Oe, and 200 Oe. The zero–field measurements performed here have the advantage that the contributions from the PM susceptibility are suppressed compared to an in–field measurement. Figure 3(b) shows $M_{\mathrm{TRM}}(T)$ measured as per the above descriptions. A clear signature of the GP-like phase is seen in the form of an upturn in magnetization at a temperature well above T_N. The T_G obtained from thermoremanent measurement is 342 K, which is close to the value of 340 K, estimated from magnetic susceptibility earlier.

C. Thermal conductivity and Raman spectroscopy

Figure 4(a) shows the thermal conductivity, $\kappa_t(T)$, of $TbFe_{0.5}Cr_{0.5}O_3$ measured in zero and in an applied magnetic field of 9 T. The overall magnitude and temperature dependence of the thermal conductivity suggest that the lattice thermal transport is dominant in this material. As can be seen from the figure, there is no appreciable change in $\kappa_t(T)$ with the application of 9 T. The relatively low value of $\kappa_t(T)$ supports the presence of disorder giving rise to the observed Griffiths-like phase. In the context of the atomic disorder in UZr^2 and its impact on heat transport behavior, it is helpful to compare the measured thermal conductivity to the theoretically achievable minimum of the lattice contribution (fully disordered structure). In this model, the $\kappa_{t(\mathrm{min})}(T)$ dependence can be calculated under Debye approximation by assuming that the transverse and longitudinal acoustic

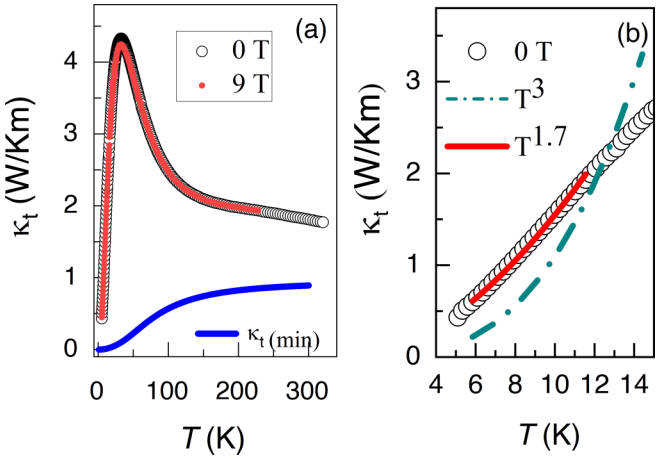

FIG. 4. (a) The variation of thermal conductivity, $\kappa_t(T)$ of $TbFe_{0.5}Cr_{0.5}O_3$ as a function of temperature. As seen, there is no appreciable change in $\kappa_t(T)$ with the application of 9 T. The magnetic anomalies at T_N and T_{SR} seen in the derivative of magnetization are not observed in $\kappa_t(T)$ or in the derivative (not shown). The blue solid line represents the minimum thermal conductivity (see text). (b) Solid and dashed lines represent $T^{1.7}$ and T^3 dependencies of $\kappa_t(T)$, respectively.

phonon modes are indistinguishable [46]. The results obtained for $TbFe_{0.5}Cr_{0.5}O_3$ using the Debye temperature, $\theta_D = 380$ K [47], and the number of atoms per unit volume, $n = 4.7528$ m^{-3}, are shown in Fig. 4(a) by a blue solid line. The magnetic anomalies that occur at T_N and T_{SR} (seen in the derivative of magnetization) are absent in the derivative of $\kappa_t(T)$ (not shown here). In general, the behavior of $\kappa_t(T)$ of $TbFe_{0.5}Cr_{0.5}O_3$ is similar to the thermal conductivity in other $RFeO_3$ compounds like $YFeO_3$, $GdFeO_3$ and $DyFeO_3$ [48]. However, in the work by Zhao *et al.* [48], single-crystal samples of orthoferrites were studied in the milli–Kelvin temperature range and in external magnetic fields up to 14 T. In earlier studies on $GdFeO_3$ and $DyFeO_3$, magnetic anomalies were also reflected in the thermal conductivity [49,50]. Significantly low *c*-axis thermal conductivity was observed in $YFeO_3$, $GdFeO_3$, and $DyFeO_3$. Considering that the present sample is polycrystalline, we observe higher values of thermal conductivity in $TbFe_{0.5}Cr_{0.5}O_3$. The total thermal conductivity could be compared to the T^3 boundary scattering limit of phonons [51]. In Fig. 4(b), the temperature dependence of the T^3 form of $\kappa_t(T)$ is shown as a dashed line. The solid line is a fit to $\kappa_t(T) \propto T^n$, where n is varied as a free parameter. A value of 1.7(3) was obtained for n. The $\kappa_t(T)$ of $DyFeO_3$ showed a weak curvature at low temperature (below 3 K) which is attributed to a magnonic contribution of Dy spin system [50]. Such a concave structure is not readily observed in the present case, however, there seems to be an indication near 2 K.

Raman spectroscopy was carried out at different temperatures to understand the phonon behavior across the magnetic anomalies seen in the susceptibility of $TbFe_{0.5}Cr_{0.5}O_3$. Raman spectra was recorded from 110 K to 300 K as shown in Fig. 5 (top panel) with the most intense mode assignment matching with $RFeO_3$ [52] and $RCrO_3$ [53]. $TbFe_{0.5}Cr_{0.5}O_3$ is an orthorhombically distorted perovskite with *Pnma* space-

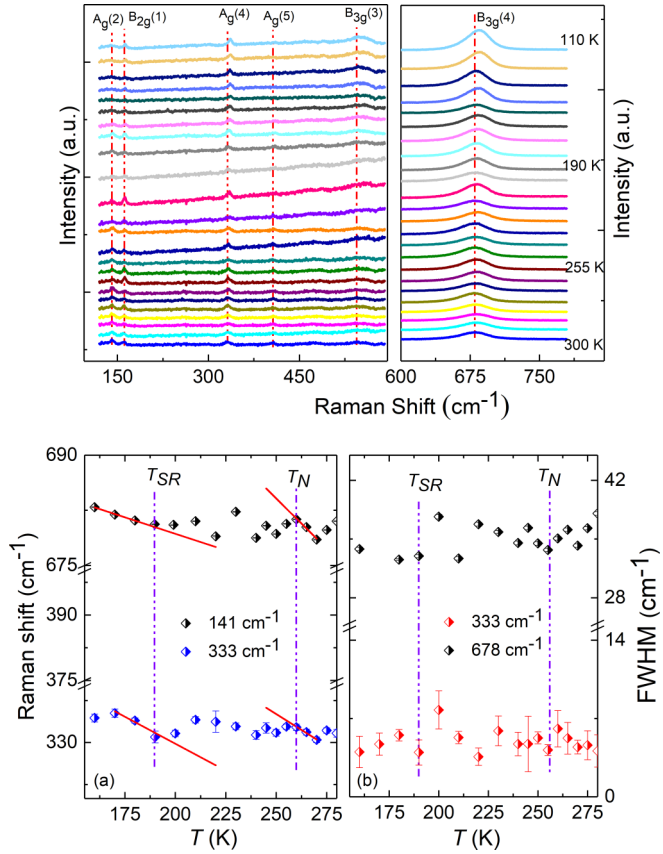

FIG. 5. Top panel: Raman spectrum of $TbFe_{0.5}Cr_{0.5}O_3$ as a function of temperature. The most intense phonon modes are assigned. Lower panel: (a) Temperature dependence of phonon frequency obtained from the fit of the spectral profile with Lorentzian function is shown. Red solid line is a fit using the anharmonic function, Eq. (1). (b) Temperature dependence of phonon linewidth. Vertical violet dashed lines in (a) and (b) mark the positions of T_N and T_{SR}.

group symmetry. The irreducible representations corresponding to the phonon modes at the BZ center [54] can be defined as $\Gamma = 7A_g + 5B_{1g} + 7B_{2g} + 5B_{3g} + 8A_u + 10B_{1u} + 8B_{2u} + 10B_{3u}$. Here, 24 $(7A_g + 5B_{1g} + 7B_{2g} + 5B_{3g})$ are the Raman active modes, 25 $(9B_{1u} + 7B_{2u} + 9B_{3u})$ are the infrared modes, A_u is an inactive mode, and three $(B_{1u} + B_{2u} + B_{3u})$ are acoustic modes. Among them, the modes which are above 300 cm^{-1} are related to the vibrations of oxygen, the modes below 200 cm^{-1} are associated with the rare-earth ions, and in the intermediate frequency range vibration patterns involve both ions [55]. However, the Raman vibrational modes corresponding to an orthorhombic structure are $A_g + B_{2g}$ and $2B_{1g} + 2B_{3g}$, which are symmetric and antisymmetric modes, respectively. In contrast, $A_g + 2B_{2g} + B_{3g}$, $2A_g + 2B_{1g} + B_{2g} + B_{3g}$, and $3A_g + B_{1g} + 3B_{2g} + B_{1g}$ are associated with the bending modes, rotation and tilt modes of the octahedra, and for the-rare earth vibrations, respectively [56]. Raman modes generally shift to low frequency as the temperature increases, accompanied by a monotonic increase in FWHM [57]. This is mainly due to the expansion of the lattice as thermal energy increases. Absence of any extra peak indicates that the spectral symmetry remains the same at all measured

temperatures, confirming that the magnetic anomalies are not associated with any structural phase transition. We analyzed the well-resolved Raman modes in detail, using a Lorentzian function. The temperature dependence of the phonon frequencies of modes $A_g(2)$ (141 cm^{-1}), $A_g(4)$ (333 cm^{-1}), and $B_{3g}(4)$ (678 cm^{-1}) along with the fit assuming a standard anharmonic dependence [58] of phonon modes are shown in Fig. 5(a).

The anharmonic dependence of the modes is given by

$$\omega_{\text{anh}}(T) = \omega_0 - C\left(1 + \frac{2}{(e^{\hbar\omega/k_B T} - 1)}\right). \quad (1)$$

Here ω_0 is temperature–independent part of linewidth, C is a constant determined from the fitting, $\hbar\omega$ is the phonon energy, and k_B is the Boltzmann constant. The deviation in the phonon frequency from anharmonic dependence near T_N and T_{SR} can be clearly seen in Fig. 5(a). Magnetostriction can also give rise to similar anomalous behavior in phonon frequency by modifying the unit cell volume [57]. But in that case, FWHM remains unchanged as it corresponds to phonon lifetime, which is not affected by subtle change in lattice volume caused by magnetostriction. But, from Fig. 5(b), it can be seen that FWHM abruptly drops near the magnetic-transition temperatures. The anomalous change in the mode frequencies and linewidths near the magnetic transition establishes the spin–phonon coupling in $TbFe_{0.5}Cr_{0.5}O_3$. Similar signatures of spin–phonon coupling were reported in $RCrO_3$ [53] and $DyFe_{0.5}Cr_{0.5}O_3$ [59]. The possible coupling mechanism involved is the phonon modulation of superexchange integral below the magnetic ordering temperature [60].

D. Neutron diffraction: Reentrant spin reorientation and short-range spin correlations

The macroscopic magnetic measurements (Sec. III B) on $TbFe_{0.5}Cr_{0.5}O_3$ explicitly suggest the antiferromagnetic ordering at T_N, the possibility of a SR transition at T_{SR}, and the presence of Griffiths-like phase. We now proceed to investigate $TbFe_{0.5}Cr_{0.5}O_3$ in detail using neutron scattering to understand the SR process and to ascertain the magnetic structures above and below the T_{SR}. For this purpose, neutron-diffraction experiments were carried out on powder samples of $TbFe_{0.5}Cr_{0.5}O_3$ at various temperatures in the range, 7.7 K to 350 K. The experimental neutron diffraction patterns at 300 K, 215 K, 100 K, 20 K, and 7.7 K are shown in Figs. 6(a)–6(e) (red circles). Orthoferrites adopt an orthorhombic structure as observed in a variety of $RFe_{0.5}Cr_{0.5}O_3$ [20]. For R = Tb, Dy, Ho, and Er, $RFe_{0.5}Cr_{0.5}O_3$ adopts a distorted orthorhombic structure and order antiferromagnetically below about 270 K in F_yG_z configuration compatible with the Γ_4 representation.

They also exhibit a SR transition from F_yG_z (Γ_4) to G_yF_z (Γ_2). If the cations order crystallographically, the perovskite may adopt a doubled unit cell with monoclinic $P2_1/n$ space group [61]. In $TbFe_{0.5}Cr_{0.5}O_3$, Rietveld analysis of the diffraction data at 350 K with $P2_1/n$ space group resulted in

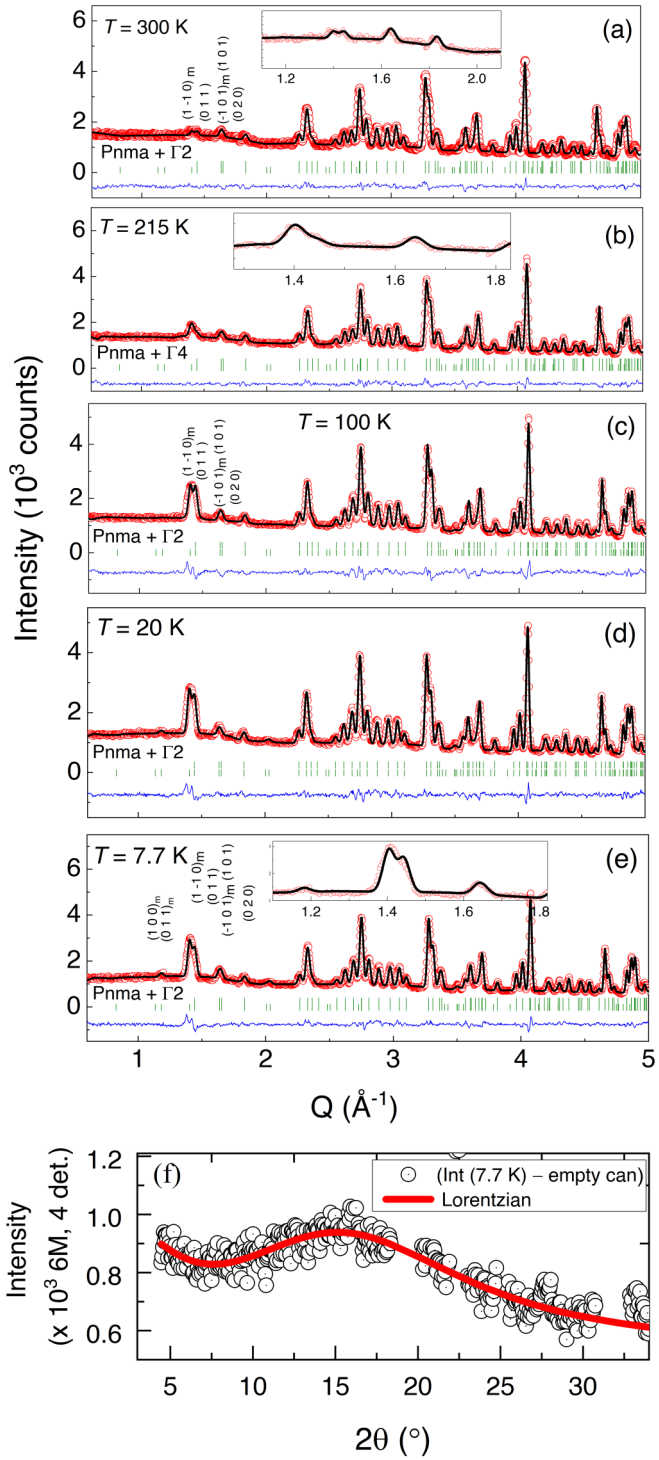

FIG. 6. (a)–(e) Rietveld refinement of the neutron powder diffraction patterns of $TbFe_{0.5}Cr_{0.5}O_3$ at 300 K, 215 K, 100 K, 20 K, and 7.7 K. There is a weak magnetic contribution even at 300 K which is above the T_N, observed in magnetometry. A magnified view of the low-Q region is provided in the inset of (a), (b), and (e). (f) Diffuse scattering intensity at 7.7 K, after subtracting the contribution from the empty can, along with a curve fit (solid line) using a Lorentzian function.

TABLE I. Structural parameters and selected bond distances and bond angles of $TbFe_{0.5}Cr_{0.5}O_3$ at different temperatures obtained from neutron diffraction. The nuclear space group is *Pnma* where the atomic positions are Tb 4*c* (*x*, *y*, *z*), Cr/Fe 4*b* (0.5, 0, 0.5), and O 4*c* and 8*d* (*x*, *y*, *z*). Long (*l*) and short (*s*) bond lengths correspond to *M*–O(2) bonds in the *ac* plane. Medium (*m*) bond length corresponds to the out–of–plane *M*– O(1) apical bond.

	350 K	300 K	215 K	100 K	20 K	7.7 K
a (Å)	5.5532(4)	5.5554(6)	5.5511(6)	5.5449(1)	5.5404(1)	5.5392(1)
b (Å)	7.6097(6)	7.6108(6)	7.6035(5)	7.5977(6)	7.5936(3)	7.5919(3)
c (Å)	5.3104(8)	5.3125(0)	5.3097(3)	5.3128(4)	5.3139(2)	5.3127(3)
Fe(Cr)–O1 (*m*) (Å)	1.9875(6)	1.9879(1)	1.9860(4)	1.9847(3)	1.9834(3)	1.9830(1)
Fe(Cr)–O2 (*l*) (Å)	2.0114(2)	2.0122(1)	2.0107(5)	2.0094(2)	2.0079(2)	2.0075(1)
Fe(Cr)–O2 (*s*) (Å)	1.9923(1)	1.9931(6)	1.9918(4)	1.9918(0)	2.0005(2)	2.0001(5)
Fe(Cr)–O1–Fe(Cr)(°)	146.3(4)	146.3(3)	146.3(2)	146.2(5)	146.3(2)	146.3(2)
Fe(Cr)–O2–Fe(Cr)(°)	147.3(1)	147.3(1)	147.3(1)	147.3(1)	146.5(1)	146.5(1)

$R_p = 3.52$, $R_{wp} = 4.61$, $R_{exp} = 2.82$, $\chi^2 = 2.67$; whereas $R_p = 2.99$, $R_{wp} = 3.89$, $R_{exp} = 2.82$, $\chi^2 = 1.9$ were obtained for *Pnma*. The *R* factor indicates a reasonably good fit with *Pnma*. However, the intensity of the nuclear Bragg peak position (101) was not fully accounted for. Even at 350 K, an appreciable contribution from magnetic scattering toward the total scattered intensity was observed as shown in the Supplemental Material, Fig. S1 [62].

To determine the magnetic structure, we scrutinized the symmetry-allowed magnetic structures for $RFeO_3$ compounds in *Pnma* space group. There exists eight irreducible representations, Γ_1 through Γ_8, listed in Kovalev tables coded in the software SARA*h* are given in Table II. For the 4*b* Wyckoff position, the configurations Γ_5 to Γ_8 are incompatible with a net magnetic moment on the Fe [1]. The *k*–search utility in FullProf was used to obtain the propagation vector of the magnetic structure. Irreducible representation analysis using $k = (0,0,0)$ leads to four possibilities, $\Gamma_1(Pnma)$, $\Gamma_2(Pn'm'a)$, $\Gamma_3(Pnm'a')$, and $\Gamma_4(Pn'ma')$. Using Bertaut's notation, these four magnetic space groups can be written as $G_xC_yA_z$, $C_xG_yF_z$, $F_xA_yC_z$, $A_xF_yG_z$, respectively, corresponding to magnetic ordering of the Cartesian components of M^{3+} spins in unit cell. But Γ_3 is not consistent with the observed strong antiferromagnetic coupling between nearest Fe neighbours.

Subsequently, SARA*h* was used to obtain the magnetic representations of the allowed magnetic structures. After testing the different possible magnetic representations along with the nuclear phase in *Pnma*, a better visual fit to the experimental data with reasonable agreement factors were obtained for Γ_2, and was accepted as the solution of the magnetic structure at 350 K (not shown here). The goodness–of–fit for the magnetic refinement, R_{mag}, for the three representations are as follows: $\Gamma_1 = 25.4$, $\Gamma_4 = 95.2$, $\Gamma_2 = 17.4$. A comparison of the refinement results for all the allowed representations are given in the Supplemental Material, Fig. S2 [63]. Figure 6(a) shows the neutron diffraction patterns at 300 K along with the refinement patterns using *Pnma* nuclear space group and the magnetic structure according to Γ_2 representation. The nuclear space group of $TbFe_{0.5}Cr_{0.5}O_3$ at all temperatures down to 7.7 K was found to be *Pnma*. The refined values of the lattice and bond parameters at different temperatures are given in Table I. Here, three different *M–O* bond lengths are listed. Long (*l*) and short (*s*) bond lengths correspond to *M–O*(2) bonds in the *ac* plane while the medium (*m*) bond length corresponds to the out-of-plane *M–O*(1) apical bond length which is almost parallel to the *b* axis.

As understood from the $M(T)$ data presented in Fig. 2(a), an anomaly occurs in $TbFe_{0.5}Cr_{0.5}O_3$ at $T_N = 257$ K. Refinement of the diffraction pattern suggests that the magnetic structure is Γ_4 ($Pn'ma'$) at 215 K, implying that the magnetic structure changes from $\Gamma_2 \rightarrow \Gamma_4$ at T_N. The refined neutron-diffraction pattern at 215 K is shown in Fig. 6(b). A second SR transition back to Γ_2 ($Pn'm'a$) is observed at 100 K. This temperature is below T_{SR} (190 K), which is identified through the derivative of magnetization curve. Further, the Γ_2 magnetic structure remains stable down to 7.7 K. The refined magnetic moment values obtained at 7.7 K are Fe^{3+}/Cr^{3+}: 0.13(1) μ_B (m_x), 3.19(4) μ_B (m_y), and 1.27(1) μ_B (m_z); and $Tb^{3+} = 1.14(2)$ (m_x). A detailed table of magnetic moments at different temperatures is provided in the Supplemental Material, Table S1 [64]. In Fig. 6(f), the neutron-diffraction pattern of $TbFe_{0.5}Cr_{0.5}O_3$ at 7.7 K is presented after subtracting the contribution from the empty vanadium can sample holder. The broad feature at low scattering angles lends support to the presence of short-range magnetic order in $TbFe_{0.5}Cr_{0.5}O_3$. Our attempt to analyze the diffuse intensity by fitting it to a Lorentzian curve is shown as a red solid line in Fig. 6(f). A spin-spin correlation length of approximately 9 Å is estimated.

TABLE II. The possible magnetic structures of $RFeO_3$ allowed for *Pnma* and *Pbnm* symmetry, where G denotes (+ − +-), F (+ + ++), A (+ − −+), C (+ + −−), O (0000). *x*, *y*, and *z* denote orientations parallel to the crystallographic directions *a*, *b*, and *c*.

	Pnma			*Pbnm*		
Irreps	Space group	4*b*	4*c*	space group	4*b*	4*c*
Γ_1	*Pnma*	$G_xC_yA_z$	C_y	*Pbnm*	$A_xG_yC_z$	C_z
Γ_2	*Pn′m′a*	$C_xG_yF_z$	C_xF_z	*Pbn′m′*	$F_xC_yG_z$	F_xC_y
Γ_3	*Pnm′a′*	$F_xA_yC_z$	F_xC_z	*Pb′nm′*	$C_xF_yA_z$	C_xF_y
Γ_4	*Pn′ma′*	$A_xF_yG_z$	F_y	*Pb′n′m*	$G_xA_yF_z$	F_z
Γ_5	*Pn′m′a′*	$O_xO_yO_z$	A_xG_z	*Pb′n′m′*	$O_xO_yO_z$	G_xA_y
Γ_6	*Pnma′*	$O_xO_yO_z$	A_y	*Pb′nm*	$O_xO_yO_z$	A_z
Γ_7	*Pn′ma*	$O_xO_yO_z$	G_y	*Pbn′m*	$O_xO_yO_z$	G_z
Γ_8	*Pnm′a*	$O_xO_yO_z$	G_xA_z	*Pbnm′*	$O_xO_yO_z$	A_xG_y

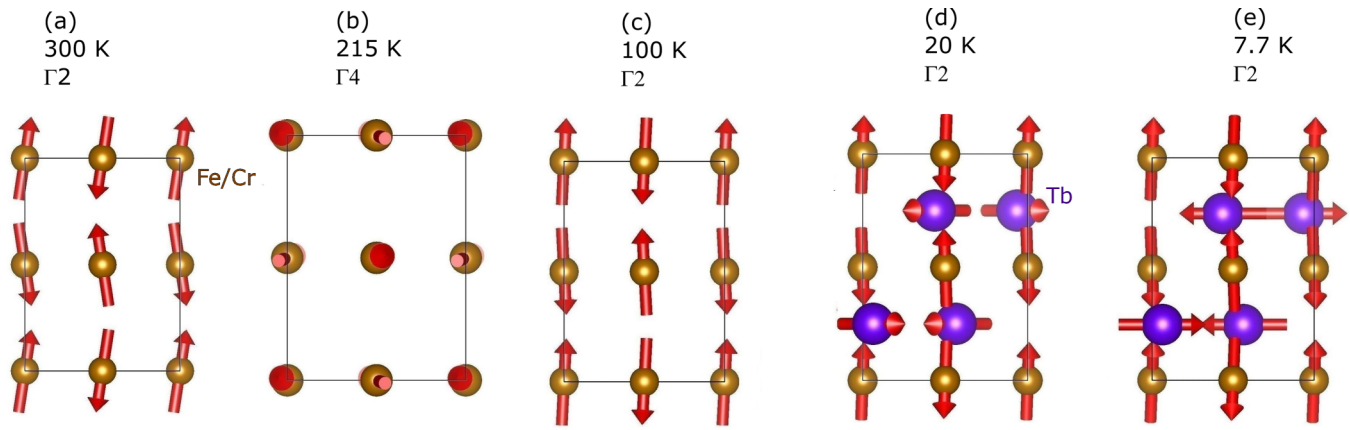

FIG. 7. The magnetic structure of $TbFe_{0.5}Cr_{0.5}O_3$ at (a) 300 K (Γ_2), (b) 215 K (Γ_4), and (c) 100 K (Γ_2). The Γ_2 structure remains stable down to 7.7 K, which was the lowest probed temperature by neutrons in this study. (d), (e) The magnetic structure at 20 K and 7.7 K, respectively (magnetic moment of Tb^{3+} is multiplied by three to make it visible).

Further, the magnetic rare earth in $RFe_{0.5}Cr_{0.5}O_3$ is reported to develop magnetic ordering at low temperatures below 15 K [20]. Our refinement of diffraction data at 20 K is consistent with the picture that Tb^{3+} moments are magnetically ordered in C_xF_z structure with a FM component along the z axis and only C_x part remains till 7.7 K. It is reported in a recent work [20] on $TbFe_{0.5}Cr_{0.5}O_3$ that only the C_y (for *Pbnm* space group) part remains whereas the FM interactions disappear with the SR at 1.9 K. As a result, diffuse magnetic scattering features emerge; this is well captured in our work as can be seen in Fig. 6(f). Direct observation of diffuse scattering in the neutron-diffraction signal suggests the presence of short-range ordering of the Tb^{3+} moments. The magnetic structures of the transition-metal and rare-earth moments as a function of temperature are shown in Fig. 7.

E. Density-functional-theory calculations

From the total energy calculations for five different collinear magnetic configurations, AFM1 (↑↓↑↓) is found to be the most stable with the lowest energy. The AFM1 spin structure is found to be consistent with our experimental observation for the Γ_2 state at 7.7 K. Similarly, the first excited AFM2 configuration is consistent with the spin structure for the Γ_4 state at 300 K whose total energy is ∼36 meV per formula unit higher compared to the AFM1 state of $TbFe_{0.5}Cr_{0.5}O_3$. The order of relative stability of the magnetic states are AFM1 > AFM2 > FIM2 > FIM1 > FM. This may be an indication of the competing ground state between AFM1 and AFM2 observed as a GP transition from Γ_2 to Γ_4 and, subsequently, the reentrant to Γ_2 phase as seen in Fig. 7. The magnetic anisotropy energy calculated is ∼4.68 meV per formula unit of $TbFe_{0.5}Cr_{0.5}O_3$with in-plane easy axes. In $TbFe_{0.5}Cr_{0.5}O_3$, the lanthanide Tb takes the charge state

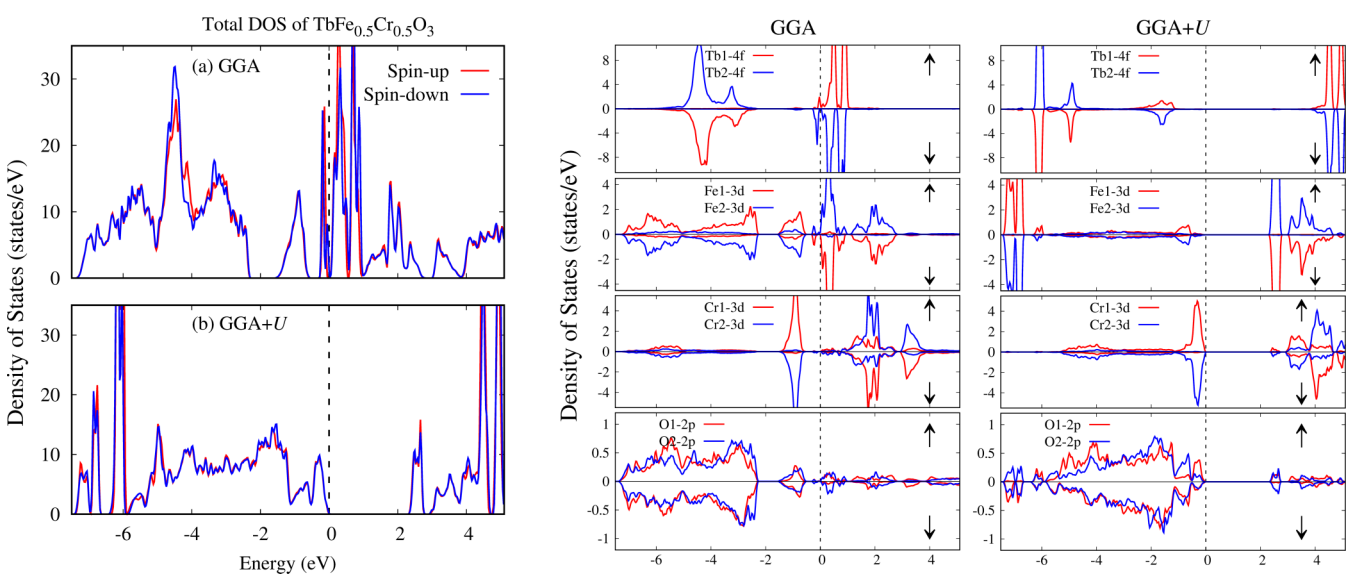

FIG. 8. Total and partial DOS of $TbFe_{0.5}Cr_{0.5}O_3$ in AFM1 configuration: Total DOS within GGA (top) and GGA+U (bottom) (left) functionals; partial DOS contributions from Tb–4f, Fe–3d, Cr–3d <, and O–2p states, respectively, within GGA (middle) and GGA+U (right) functionals for the spin–up and spin–down channels.

3+ with $4f^8$ configuration. Likewise, the transition-element Fe nominally takes the charge state 3+ with $3d^5$ and Cr with charge state 3+ should take the $3d^3$ configurations, respectively. In the stable AFM1 state, the calculated spin moment at each site of Tb, Fe, and Cr are $\pm 5.9\ \mu_B$, $\pm 3.65\ \mu_B$, and $\pm 2.36\ \mu_B$, respectively. Their respective orbital moments are $\pm 1.03\mu_B$, $\pm 0.05\mu_B$, and $\mp 0.034\mu_B$, respectively. With GGA+U effects, the spin moment of Tb, Fe, and Cr turns out to be $\pm 5.97\mu_B$, $\pm 4.14\mu_B$, and $\pm 2.57\mu_B$, respectively. The total magnetic moment compensates to zero as Tb, Fe, and Cr couples antiferromagnetically among each other as observed in Fig. 7.

We now proceed to the electronic structure of $TbFe_{0.5}Cr_{0.5}O_3$in AFM1 state within GGA and GGA+U, respectively. The spin-resolved total and partial density of states (DOS) are shown in Fig. 8. $TbFe_{0.5}Cr_{0.5}O_3$is found to be insulating with a band gap of ~0.12 (2.4) eV within GGA (GGA + U). The correlation effects U significantly change the electronic behavior. As seen in the partial DOS, the main contributions from Tb–4f states that were observed around E_F are shifting away from each other.

Those states that are fully occupied shift deep in the valence region while the unoccupied state moves far away in the conduction region. Similar features were also observed for Fe–3d states around E_F. On the other hand, Cr–3d states are contributing at and around E_F, hybridizing strongly with the O–2p orbitals (see partial DOS in Fig. 8). This is mainly due to the hybridization between the 3d states of Cr and Fe with the O–2p states. From the partial DOS contributions of Fe–3d, three t_{2g} and two e_g are fully occupied by five electrons in spin up, but in Cr–3d, three t_{2g} are fully occupied in the spin-up channel while e_g bands are empty.

IV. CONCLUSIONS

We observe an antiferromagnetic transition T_N at 257 K and a SR transition T_{SR} at 190 K in the orthoferrite $TbFe_{0.5}Cr_{0.5}O_3$. Interestingly, a reentrant SR is seen in this compound, where the spins reorient again at 100 K. Through detailed neutron-diffraction experiments and analysis, we find that the spin structure changes from the Γ_2 representation at 350 K to Γ_4 at 215 K and then reverts to Γ_2 at 100 K. This structure remains stable until 7.7 K. A clear signature of GP is observed in the magnetization response of $TbFe_{0.5}Cr_{0.5}O_3$ and also short-range spin fluctuations that extend up to high temperature. $TbFe_{0.5}Cr_{0.5}O_3$ exhibits low thermal-conductivity values, suggesting disordered cation arrangement which supports the Griffiths-like phase; and is not perturbed by the application of external magnetic field up to 9 T. The magnetic anomalies at T_N and T_{SR} are not directly seen in the thermal conductivity data, but the latter is dominated by the phonon contributions. Raman spectroscopic investigation reveals clear evidence of spin-phonon coupling in this compound.

ACKNOWLEDGMENTS

The authors acknowledge the Center for Nano Science and Engineering (CeNSE), Indian Institute of Science, Bengaluru. B.M. acknowledges financial support from University Grants commission (UGC-531996), India for Senior Research fellowship (SRF). H.S.N. acknowledges a faculty start-up grant from UTEP and a Rising Stars award. Work at INL was supported by DOE's Early Career Research Program. M.P.G. acknowledges the Higher Education Reform Project (HERP DLI-7B) of Tribhuvan University, Kirtipur, Nepal for the start-up grant, and Alexander von Humboldt Foundation, Germany for the partial support as a return fellowship. S.R.B. thanks NAST, Nepal for the Ph.D. fellowship and IFW-Dresden for funding during a research stay in Germany. M.P.G. and S.R.B. thank Manuel Richter for the fruitful discussion and Ulrike Nitzsche for technical assistance.

[1] R. L. White, J. Appl. Phys. **40**, 1061 (1969).
[2] A. V. Kimel, C. D. Stanciu, P. A. Usachev, R. V. Pisarev, V. N. Gridnev, A. Kirilyuk, and T. Rasing, Phys. Rev. B **74**, 060403(R) (2006).
[3] A. V. Kimel, A. Kirilyuk, A. Tsvetkov, R. V. Pisarev, and T. Rasing, Nature **429**, 850 (2004).
[4] J. Jiang, Z. Jin, G. Song, X. Lin, G. Ma, and S. Cao, Appl. Phys. Lett. **103**, 062403 (2013).
[5] A. V. Kimel, B. A. Ivanov, R. V. Pisarev, P. A. Usachev, A. Kirilyuk, and T. Rasing, Nat. Phys. **5**, 727 (2009).
[6] Y. Tokunaga, N. Furukawa, H. Sakai, Y. Taguchi, T.-H. Arima, and Y. Tokura, Nat. Mater. **8**, 558 (2009).
[7] T. Yamaguchi, J. Phys. Chem. Solids **35**, 479 (1974).
[8] S. Artyukhin, M. Mostovoy, N. P. Jensen, D. Le, K. Prokes, V. G. de Paula, H. N. Bordallo, A. Maljuk, S. Landsgesell, H. Ryll *et al.*, Nat. Mater. **11**, 694 (2012).
[9] J. E. Bourée and J. Hammann, J. Phys. France **36**, 391 (1975).
[10] E. Bertaut, J. Chappert, J. Mareschal, J. Rebouillat, and J. Sivardière, Solid State Commun. **5**, 293 (1967).
[11] J. Tejada, X. X. Zhang, A. Roig, O. Nikolov, and E. Molins, Europhys. Lett. **30**, 227 (1995).
[12] H. Taguchi, J. Solid State Chem. **131**, 108 (1997).
[13] A. Dahmani, M. Taibi, M. Nogues, J. Aride, E. Loudghiri, and A. Belayachi, Mater. Chem. Phys. **77**, 912 (2003).
[14] J. B. Goodenough, Phys. Rev. **100**, 564 (1955).
[15] J. D. Gordon, R. M. Hornreich, S. Shtrikman, and B. M. Wanklyn, Phys. Rev. B **13**, 3012 (1976).
[16] E. Bertaut, J. Mareschal, and G. D. Vries, J. Phys. Chem. Solids **28**, 2143 (1967).
[17] E. Bertaut, J. Mareschal, G. De Vries, R. Aleonard, R. Pauthenet, J. Rebouillat, and V. Zarubicka, IEEE Trans. Magn. **2**, 453 (1966).
[18] H. Nhalil, H. S. Nair, S. R., A. M. Strydom, and S. Elizabeth, J. Appl. Phys. **117**, 173904 (2015).

[19] Y. Fang, Y. Yang, X. Liu, J. Kang, L. Hao, X. Chen, L. Xie, G. Sun, V. Chandragiri, C.-W. Wang *et al.*, Sci. Rep. **6**, 33448 (2016).
[20] J. P. Bolletta, F. Pomiro, R. D. Sánchez, V. Pomjakushin, G. Aurelio, A. Maignan, C. Martin, and R. E. Carbonio, Phys. Rev. B **98**, 134417 (2018).
[21] N. Fairley and C. S. Ltd., CasaXPS 2.3.15: CasaXPS processing software for XPS spectra (2009), http://www.casaxps.com.
[22] H. M. Rietveld, J. Appl. Crystallogr. **2**, 65 (1969).
[23] J. Rodríguez-Carvajal, Physica B: Condensed Matter **192**, 55 (1993).
[24] A. Wills, Physica B: Condensed Matter **276-278**, 680 (2000).
[25] P. Blaha, K. Schwarz, G. K. Madsen, D. Kvasnicka, and J. Luitz, *An Augmented Plane Wave+ Local Orbitals Program for Calculating Crystal Properties* (Vienna University of Technology, Austria, 2001).
[26] J. P. Perdew, K. Burke, and M. Ernzerhof, Phys. Rev. Lett. **77**, 3865 (1996).
[27] V. I. Anisimov, F. Aryasetiawan, and A. I. Lichtenstein, J. Phys.: Condens. Matter **9**, 767 (1997).
[28] M. P. Ghimire, L.-H. Wu, and X. Hu, Phys. Rev. B **93**, 134421 (2016).
[29] M. P. Ghimire and X. Hu, Mater. Res. Express **3**, 106107 (2016).
[30] M. P. Ghimire, Sandeep, and R. K. Thapa, Mod. Phys. Lett. B **24**, 2187 (2010).
[31] Y. Yuan, H. L. Feng, M. P. Ghimire, Y. Matsushita, Y. Tsujimoto, J. He, M. Tanaka, Y. Katsuya, and K. Yamaura, Inorg. Chem. **54**, 3422 (2015).
[32] H. L. Feng, S. Calder, M. P. Ghimire, Y.-H. Yuan, Y. Shirako, Y. Tsujimoto, Y. Matsushita, Z. Hu, C.-Y. Kuo, L. H. Tjeng *et al.*, Phys. Rev. B **94**, 235158 (2016).
[33] H. L. Feng, M. P. Ghimire, Z. Hu, S.-C. Liao, S. Agrestini, J. Chen, Y. Yuan, Y. Matsushita, Y. Tsujimoto, Y. Katsuya *et al.*, Phys. Rev. Mater. **3**, 124404 (2019).
[34] G. C. Allen, M. T. Curtis, A. J. Hooper, and P. M. Tucker, J. Chem. Soc., Dalton Trans. **16**, 1675 (1973).
[35] G. C. Allen, M. T. Curtis, A. J. Hooper, and P. M. Tucker, J Chem. Soc., Dalton Trans. **14**, 1525 (1974).
[36] B. D. Padalia, W. C. Lang, P. R. Norris, L. M. Watson, and D. J. Fabian, Proc. R. Soc. London. Series A: Math. Phys. Sci. **354**, 269 (1977).
[37] C. Kittel, *Introduction to Solid State Physics* (Wiley, New York, 2004).
[38] R. B. Griffiths, Phys. Rev. Lett. **23**, 17 (1969).
[39] H. S. Nair, D. Swain, H. N., S. Adiga, C. Narayana, and S. Elizabeth, J. Appl. Phys. **110**, 123919 (2011).
[40] T. Chakraborty, H. S. Nair, H. Nhalil, K. R. Kumar, A. M. Strydom, and S. Elizabeth, J. Phys.: Condensed Matter **29**, 025804 (2016).
[41] A. K. Pramanik and A. Banerjee, Phys. Rev. B **81**, 024431 (2010).
[42] A. K. Pramanik and A. Banerjee, J. Phys.: Condens. Matter **28**, 35LT02 (2016).
[43] C. Magen, P. A. Algarabel, L. Morellon, J. P. Araújo, C. Ritter, M. R. Ibarra, A. M. Pereira, and J. B. Sousa, Phys. Rev. Lett. **96**, 167201 (2006).
[44] W. Jiang, X. Zhou, G. Williams, Y. Mukovskii, and R. Privezentsev, J. Appl. Phys. **107**, 09D701 (2010).
[45] R. Mathieu, P. Jönsson, D. N. H. Nam, and P. Nordblad, Phys. Rev. B **63**, 092401 (2001).
[46] D. G. Cahill and R. Pohl, Solid State Commun. **70**, 927 (1989).
[47] M. Vagadia, S. Rayaprol, and A. Nigam, J. Alloys Compd. **735**, 1031 (2018).
[48] J. Y. Zhao, Z. Y. Zhao, J. C. Wu, H. S. Xu, X. G. Liu, X. Zhao, and X. F. Sun, AIP Adv. **7**, 055806 (2017).
[49] Z. Y. Zhao, X. M. Wang, C. Fan, W. Tao, X. G. Liu, W. P. Ke, F. B. Zhang, X. Zhao, and X. F. Sun, Phys. Rev. B **83**, 014414 (2011).
[50] Z. Y. Zhao, X. Zhao, H. D. Zhou, F. B. Zhang, Q. J. Li, C. Fan, X. F. Sun, and X. G. Li, Phys. Rev. B **89**, 224405 (2014).
[51] R. Berman and P. G. Klemens, Phys. Today **31**(4), 56 (1978).
[52] M. C. Weber, M. Guennou, H. J. Zhao, J. Íñiguez, R. Vilarinho, A. Almeida, J. A. Moreira, and J. Kreisel, Phys. Rev. B **94**, 214103 (2016).
[53] V. S. Bhadram, B. Rajeswaran, A. Sundaresan, and C. Narayana, Europhys. Lett. **101**, 17008 (2013).
[54] S. Venugopalan, M. Dutta, A. K. Ramdas, and J. P. Remeika, Phys. Rev. B **31**, 1490 (1985).
[55] M. K. Singh, H. M. Jang, H. C. Gupta, and R. S. Katiyar, J. Raman Spectrosc. **39**, 842 (2008).
[56] M. N. Iliev, M. V. Abrashev, H.-G. Lee, V. N. Popov, Y. Y. Sun, C. Thomsen, R. L. Meng, and C. W. Chu, Phys. Rev. B **57**, 2872 (1998).
[57] A. Nonato, B. S. Araujo, A. P. Ayala, A. P. Maciel, S. Yanez-Vilar, M. Sanchez-Andujar, M. A. Senaris-Rodriguez, and C. W. A. Paschoal, Appl. Phys. Lett. **105**, 222902 (2014).
[58] M. Balkanski, R. F. Wallis, and E. Haro, Phys. Rev. B **28**, 1928 (1983).
[59] L. H. Yin, J. Yang, R. R. Zhang, J. M. Dai, W. H. Song, and Y. P. Sun, Appl. Phys. Lett. **104**, 032904 (2014).
[60] E. Granado, A. García, J. A. Sanjurjo, C. Rettori, I. Torriani, F. Prado, R. D. Sánchez, A. Caneiro, and S. B. Oseroff, Phys. Rev. B **60**, 11879 (1999).
[61] M. T. Anderson, K. B. Greenwood, G. A. Taylor, and K. R. Poeppelmeier, Prog. Solid State Chem. **22**, 197 (1993).
[62] See Supplemental Material at http://link.aps.org/supplemental/10.1103/PhysRevB.102.014418 for neutron diffraction data at 350 K with a Rietveld refinement using purely nuclear model.
[63] See Supplemental Material at http://link.aps.org/supplemental/10.1103/PhysRevB.102.014418 for Rietveld refinement at 300 K, 215 K, 100 K, 20 K, and 7.7 K for all possible irreducible representations.
[64] See Supplemental Material at http://link.aps.org/supplemental/10.1103/PhysRevB.102.014418 for the values of refined magnetic moments at different temperatures obtained from the analysis of neutron diffraction data.